

Abstract

15
16 Evolving preferential dissolution channels are common features formed during reac-
17 tive fluid flow in carbonate rocks. Understanding these is of particular importance
18 in applications involving subsurface engineered reservoirs but predicting their pro-
19 gression is currently challenging and poorly understood. Here, we propose a new
20 approach to predict both the spatial distribution and extent of dissolution using
21 a combination of experimental work, X-ray microtomography (μ CT) and machine
22 learning. We have conducted experiments, under reservoir conditions of temperature
23 and pressure, involving pre- and post-flooding μ CT characterisations, and coupled
24 the outputs with a neural network to predict locations where carbonate was most
25 likely to be dissolved. Our simulations demonstrate that our new solution can iden-
26 tify the key geometrical features that are important during dissolution, and can
27 accurately predict the location and spread of dissolution. An important benefit of
28 this approach is that it can accurately predict dissolution channels through forward
29 prediction, while it does not require further chemical parameters, using instead
30 common and accessible variables.

1 Introduction

32 Injection of fluid into carbonate reservoir rocks is a widely used process in-
33 volved in subsurface engineered reservoirs to manage permeability and fluid flow
34 (geothermal, groundwater management, carbon sequestration, enhanced oil recov-
35 ery, etc.). The injected fluid creates changes in the fluid dynamic and stress state,
36 leading to dissolution where the pore network, chemistry, temperature, fluid compo-
37 sition and pressures all influence the location, degree, and spread of the preferential
38 channelling (Hoefner & Fogler, 1988; C. N. Fredd & Fogler, 1998; Golfier et al.,
39 2002; Menke et al., 2017). The reactive and heterogeneous nature of carbonates
40 make predictions of fluid behaviour challenging, and much work has been done on
41 channelisation and classification in a variety of fluid-mineral systems as a function
42 of the fluid flow rate and the fluid properties (Hoefner & Fogler, 1988; Steefel &
43 Lasaga, 1990; Frick et al., 1994; Bazin et al., 1995; C. Fredd et al., 1996; C. N. Fredd
44 & Fogler, 1998; Golfier et al., 2002; Walle et al., 2015), where fluid properties have
45 been identified as largely controlling dissolution and channelisation in carbonates
46 (Golfier et al., 2002). Numerical modelling studies have attempted to recreate these

47 dissolution processes by including variables influencing the general shape and spread
48 of the dissolution footprint, such as system pressure, permeability, velocity of the
49 fluid, or diffusion rate across boundary layers. Models have been tested, from a
50 conceptual approach that considered a pre-existing cylindrical wormhole (Hung et
51 al., 1989; Wang et al., 1993; Buijse et al., 1997; Huang et al., 1997, 1999), to more
52 complex approaches focusing on the grain scale (Hoefner & Fogler, 1988; Daccord et
53 al., 1989), on the fluid mechanics (Daccord, Lenormand, & Lietard, 1993; Daccord,
54 Lietard, & Lenormand, 1993), or the mass and flow transfer (Liu et al., 1997; Chen
55 et al., 1997). Most of these approaches displayed reasonable qualitative results of
56 channel geometry and were backed by experimental outputs, against computation-
57 ally expensive treatments operating over millimetre scale volumes. Here, we have
58 coupled experimental work and Artificial Neural Networks (ANNs). The benefit of
59 ANNs stems from the non-linear aspect of the solving algorithms coupled with their
60 ability to learn and recognise patterns (Basheer & Hajmeer, 2000). Although stud-
61 ies have joined μ CT imaging and machine learning as a segmentation tool for 3D
62 volumes (Cortina-Januchs et al., 2011; Chauhan et al., 2016) and for rock modulus
63 estimations (Sonmez et al., 2006), no work has been published on predictions of the
64 spatial distribution of carbonate dissolution, purely relying on μ CT images. Our
65 approach has the advantage that it works as a predictive tool for channel spatial dis-
66 tribution, spread, and magnitude, over centimetre large volumes, in relatively short
67 computational times. We have combined experimental data with an ANN to develop
68 a predictive tool for preferential flow-path development.

69 The model presented in this study used datasets that were generated during exper-
70 imental investigations of reactive fluid flow in carbonate samples. We investigated
71 channels development through carbonate samples of heterogeneous nature by com-
72 paring the ANN computed solutions to 4 experimental results. For the experimental
73 fluid flows, we used a range of flow rates and these have been named High Flow
74 Rate 1 and 2 (*HFR 1*; *HFR 2*), Medium Flow Rate (*MFR*), and Low Flow Rate
75 (*LFR*). Our coupled numerical work included a pre-processing of pre-experimentally
76 tested core samples μ CT-scans followed by a training of the ANN against the post-
77 experimental channels data. The pre-experimental data - referred to as Input data
78 - were based on $18 + 1$ variables describing the geometrical attributes of the pore
79 network (steps A and B in Figure 1). The differential result between pre- and post-

80 experimental μ CT-scans allowed to pinpoint dissolution channels, leading to the
 81 generation of the Signature dataset (steps C and D in Figure 1). We trained multi-
 82 ple hidden layer ANNs on six datasets (including Input and Signature datasets) and
 83 blindly predicted on two (including the Input dataset only), corresponding to the
 84 four experimental regimes (further explained in Section 2.1). By doing so, we have
 85 been able to favourably predict the occurrence, shape, and magnitude of the disso-
 86 lution pathways evolution in heterogeneous carbonate rocks using only attributes
 87 extracted from μ CT scans, before flooding, on representative volumes. Moreover,
 88 the processing times of our solution were significantly smaller than the various
 89 computationally expensive systems models (Budek & Szymczak, 2012), with the
 90 non-negligible advantage of using larger cuboids inputs (Blunt et al., 2013; Bijeljic et
 91 al., 2004).

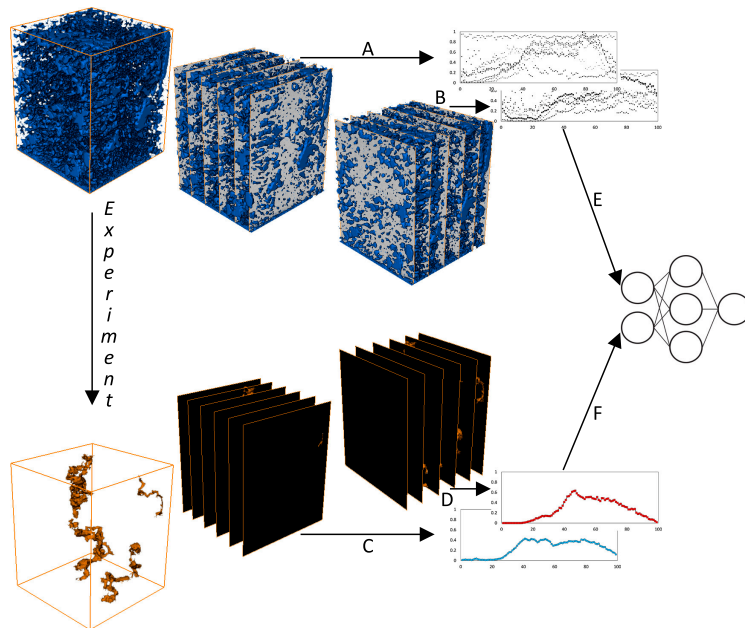


Figure 1: Data acquisition workflow. The two sub-sampled cuboids (pre-flooding and channels) are of the same size. Both stacks have been re-sliced a hundred times in two orthogonal directions. A & B: input data acquisition; C & D: signature data (or true solution) acquisition; E & F: input and signature data as attributes for the ANN.

2 Materials and Methods

2.1 Experimental matrix and dissolution regimes

The experimental dataset used to develop our methodology, and train and test the ANN, comprised a set of four experiments on highly heterogeneous - in poropermeability - travertine samples. Each core was 3.8 cm in diameter and differing in length ($6.8 \text{ cm} < L < 8.1 \text{ cm}$). The experimental procedure started with a pre-experimental preparation and conditioning of the core samples, followed by μCT acquisitions of the clean cores. The post-experimental process consisted of sonicating the samples in distilled water, before drying them for a week at $65 \text{ }^\circ\text{C}$ for one week, followed by post-experimental μCT acquisitions. The experimental flooding consisted in injecting an artificially made seawater of known pH (cf. supplementary information). The four experiments were carried under realistic geo-reservoir conditions of pressure and temperature (temperature $T = 60 \text{ }^\circ\text{C}$). The effective stress used in this study refers to the work of Terzaghi (1951), while the pore volume rate (PV_{rate}) used in this study is described by: $PV_{rate} = Q(t)/V_p$, with $Q(t)$ the amount of fluid injected per minute logged (m^3) and V_p the volume of pore of the rock sample (m^3). The porosity is calculated before the experiments, using the triple weighing technique (Luquot et al., 2016), and displays an average value of $\sim 11 \%$ (from $\sim 5 \%$ to $\sim 14 \%$). Table 1 presents the four experimental scenarios.

Experiment	Flow rate (cm^3/min)	PV_{rate} (-)	Eff. stress (MPa)	Conf. pressure (MPa)
HFR 1	15.58	2.6	10	50
HFR 2	14.25	2.5	40	50
MFR	6.24	1	10	50
LFR	1	0.2	40	50

Table 1: Flow rate, pore volume rate, effective pressure and confining pressure used for the four experimental floodings. Further petrophysical and chemical data on the rock samples are given in supplementary information.

2.2 μ CT Processing

2.2.1 Data Acquisition

For each core, pre- and post-experimental flooding, tomographic data were acquired at 130 kV, and 25 W target power loading. Each dataset consists of 2,000 projections; each of 2 s duration, during a 360° revolution. Reconstruction by filtered back-projection used Octopus v8.7 software (Dierick et al., 2004), while post-processing data analysis and registrations of the pre- and post-flooding dataset of each rock, followed by the processing of the differences between both stacks were done using Fiji (Schindelin et al., 2012) and Avizo[®]9 functions.

2.2.2 Channel Resolution

The channels formed during our experimental fluid flooding can be detected through image processing by processing the difference between the pre- and post-experimental μ CT volumes, while taking into account the initial porosity. The two types of datasets were generated. The first one represented the 3D volumes of pre-experimental scans - referred to as input data. These datasets were used for training the ANN and/or predicting the preferential pathway(s) location and magnitude. The second one were 3D volumes of dissolution channels - referred to as signature data. These datasets represent the true solution of channel(s) formation and were used for training the ANN.

As a way to account for the difference in samples sizes, we sub-sampled the 3D stacks into cuboids of variable side lengths (550 px to 650 px large) and constant axial length of 710 slices (\sim 2.5 cm by \sim 2.9 cm). Both input and signature volumes of a single core sample are sub-sampled at the same location: To save further computational time, the 3D sub-sampled volumes were re-sliced a hundred times in two orthogonal directions - each sampled direction creating a dataset which we treated as independent - with respect to the axial axis and the original orientation of the sample within the sub-sampled core. Figure 1 presents the workflow for μ CT data acquisition. In total, we have scanned four samples, translated into eight datasets, which were later divided into training & validation data (six datasets) and blind test data (two datasets) when developing the ANN.

141 **2.3 Modelling**

142 **2.3.1 Input Data**

143 The input data were a set of calculated geometric, physical, and simple statis-
144 tical variables for predicting material loss during experimental floodings. Extraction
145 of the information involved a conversion from the 16-bit grayscale 2D slices stacks to
146 normalized 1D variables that can be evaluated by the ANN.

147 The formatting of the input data has been done via a Visual Basic for Applications
148 (VBA) batch coupled with Corel[®] X7 suite has been used as a quick way to apply
149 the same formatting to each 2D slice. The batch automatically and sequentially
150 thresholded, smoothed, vectorized, and resized each image to its original size.

151 For each formatted 2D slice, a set of nineteen relevant variables were collected
152 through an in-depth image analysis. Most variables can easily be explained through
153 image interpretation and simple mathematics (1, 6, 7, 9, 10, 13, 14, 15, 17), as well
154 as variable 18 (PV_{rate} , cf. Section 2.1). The remaining variables (2, 3, 4, 5, 8, 11,
155 12, 16, 19) have been calculated using a bespoke pre-processor which performed cal-
156 culations on the equivalent elliptical shapes of each pore and the pore network (cf.
157 supporting information). Figure 2 presents a simplified workflow for pore network
158 generation. The rationale behind the use of a 2D network of pores rather than a 3D
159 pore network skeletonization enables the network to operate on a desktop, where our
160 networking software could extract a simplified set of 2D attributes which highlighted
161 the key characteristics encountered during a 3D analysis. Studies have simplified the
162 complex structure of the pores by the ellipse equivalent shape of a pore (Fournier
163 et al., 2011), while Tsukrov (Tsukrov & Kachanov, 1993) demonstrated that elon-
164 gated pores could be replaced by their ellipse-equivalent shape for DEM modelling.
165 This network, generated for each scanned slice, was based on the arrangement and
166 overlapping state of the 2D porosity: Each pore of a 2D slice was replaced by an
167 ellipse of equivalent area, shape, and orientation. These ellipses were then enlarged
168 by a constant factor. This enlarging factor, called the *area of influence*, was a com-
169 putational way of representing the hydrogeological influence of a pore around its
170 neighbourhood; or the numerical way of imaging the 3D influence of a pore on a 2D
171 slice. The 2D arrangement of a set of links symbolized a pore network. A link set
172 between two pores suggested the potential existence of a pathway between these two

173 pores in the rock. The analysis of this pore network allowed the calculation of the
 174 variables 2, 3, 4, 5, and 19, while the analysis of the ellipses defined the variables 8,
 175 11, 12, and 16.

176 *2.3.1.1 Pore network analysis (variables 2, 3, 4, 5, 19)*

177 Variables 2, 3, 4, 5, and 19 are determined as follows: the area of connected
 178 pores (2) is the sum of the 2D area of the pores which are part of a connected net-
 179 work. The total (3), median (4) and mean length connection (5) are basic math-
 180 ematical calculations using the length of every link from a 2D slice. Finally, the
 181 I/O connection (19) is a variable which is not part of the variables processed by the
 182 ANN, but rather an independent measurement used in determining the potential
 183 breakthrough location. A recursive function analyses the 2D network of links, and
 184 detects if at least one path between bottom to top of the image is found.

185 *2.3.1.2 Ellipse analysis (variables 8, 11, 12, 16)*

186 The ellipse shape of a pore can resolve the following variables: the ratio of pore
 187 area (8) represents the ratio between the area of the largest pore over the mean pore
 188 area of a 2D slice. This variable is used for excluding large outliers. Both the small
 189 (11) & the large (12) ellipse perimeter are calculations of both the ellipse shape of a
 190 pore and its enlarged version. The mean aspect ratio (16) is represented by the ratio
 191 of the minor axis b over the major axis a of an ellipse.

192 *2.3.2 Signature Data Pre-processing*

193 The signature data refers to the estimated channels magnitudes and locations.
 194 This dataset was computed from the differential result between the pre- and post-
 195 experimental scans. Our methodology involved a registration of both unaltered and
 196 altered datasets into the same 3D space, allowing us to further subtract both stacks
 197 in order to account for potential differences. Isolating and computing the dissolu-
 198 tion channels and sub-sampling has been done under Avizo [®]9. The cuboids were
 199 re-sliced and thresholded using the Fiji *AutoThresholding* function (Schindelin et
 200 al., 2012; Ridler et al., 1978). The percentage of black and white area was calcu-
 201 lated for each 2D slice using a batch code based on the *Measure* function under Fiji
 202 (Schindelin et al., 2012), and was used as the true solution of the channel shape and
 203 size for a set of slices of the 3D stack. The signature data were finally normalized

204 so that the maximum percentage area of white equals 1 (presence of dissolution
205 channel) while the minimum was equal or close to 0 (no dissolution detected).

206 ***2.3.3 Regression and Neural Network Modelling***

207 In this work, we trained both linear regressions and multiple hidden layer
208 ANNs on six datasets and predicted on two, which corresponded to the four ex-
209 perimental regimes as explained in Section 2.1. With this network trained, we
210 then predicted the remaining two, blind datasets' spatial channel signatures, cor-
211 responding to the remaining experimental regimes. For the four combinations of
212 three training experimental regimes (six datasets) and one blind test experimental
213 regime (two datasets), we performed a linear regression where eighteen normalized
214 features were input and fitted to minimize the least-squares misfit when compared to
215 the measured spatial channel signature extracted from before and after μ CT scans,
216 as described in Section 2.3. We did not perform any regression or model training
217 using the I/O variable (19), which was held aside for comparison, as seen in Section
218 2.3.1. After the linear regression was parametrized, we performed modelling using
219 an ANN based on the MATLAB's Deep Learning Toolbox (Hudson Beale et al.,
220 2018), with three hidden layers, consisting of 11, 8, and 5 neurons respectively. All
221 eighteen variables were normalized, as discussed in Section 2.3.1, before inputting
222 into the network. All transfer functions between the input and all hidden layers in
223 the ANN were hyperbolic tangent functions. The transfer function between the last
224 hidden layer and the output layer was linear. Our experimental aim was to train the
225 ANN on three experimental regimes (six datasets; three rocks), and predict channel
226 formation on a fourth experimental regime (two datasets; one rock).

227 We have randomly partitioned the data from six training datasets into 74% training
228 data and 26% validation data. We trained an ANN given this random partitioning
229 of training and validation data and forward-modelled the spatial channel signature
230 on the remaining two blind test datasets. This workflow has been repeated 3,000
231 times independently, each time training a new network given a different random par-
232 titioning of training and validation data from the same six datasets, and produced
233 3,000 predictions of the two blind datasets' spatial channel signatures. This amount
234 of iteration allowed to obtain large enough outputs in reasonably short computing
235 times (half a day for ANN training over 3,000 iterations, while predicting processing

236 was done within minutes). These 3,000 predictions have been made into a density
 237 plot which shows the most likely spatial channel signature, as well as the sensitivity
 238 of the network to the partitioning of input data into test and validation datasets.
 239 We performed this workflow for all four combinations of three training experimen-
 240 tal regimes (six datasets) and one prediction experimental regime (two datasets),
 241 allowing us to simulate four, independent experiments.

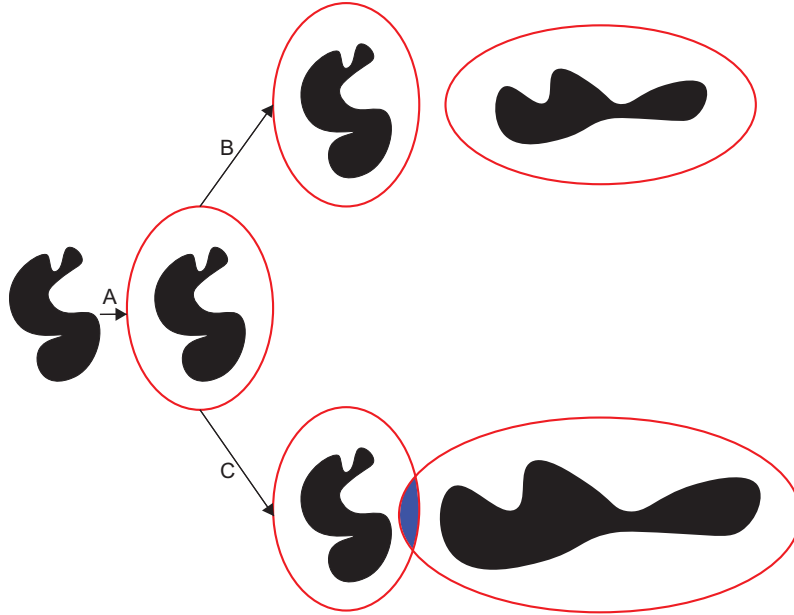


Figure 2: Steps for the detection of a link between two pores (black shapes), virtually representing a suspected connection between two pores in a rock. The step (A) represents the area of influence applied around a pore through a multiplier of the original pore area. Case (B) shows two non-overlapping pores. Case (C) displays a case of overlapping ellipses.

242 3 Results

243 3.1 Example of Post-experimental μ CT Results

244 Figure 3 presents an example of signature from two datasets (blue curve; cf.
 245 steps C and D in Figure 1) plotted under their corresponding channel. The back-
 246 ground greyscale images are the last image from the image stack in the Y-axis (left)
 247 and X-axis (right), and are displayed in a way to contextualize the channels in their

248 volumes. The cross-plotting of the thresholded percentage area of black to white of a
 249 channel offers a good insight into the location, the spread, and the magnitude of the
 250 created pore space. The values of the signature data were cross-normalized between
 251 datasets.

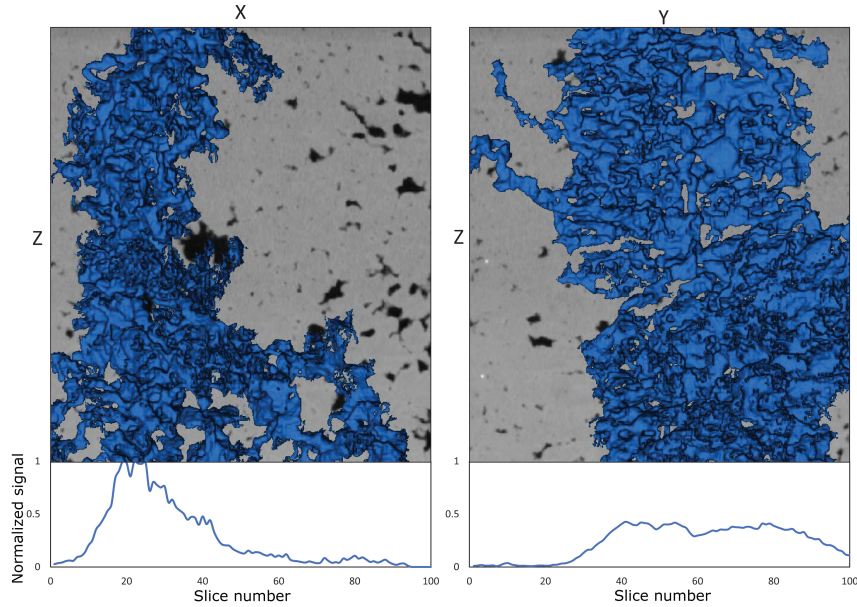


Figure 3: Example of signatures plotted under their respective cross-sectional direction for the *HFR* 1 experiment. Left: XZ direction; Right: YZ direction. The blue volumes represent the material removed after fluid flow through the core sample, while the plot underneath each graph represents the intensity of this material removal, per direction.

252 3.2 ANN Outputs

253 The predicted spatial channel signatures from the fitted linear regression mod-
 254 els, as seen in Figure 5, are displayed as white curves, with the signatures measured
 255 from μ CT scans displayed as red curves. Table 3 shows the percentage decrease in
 256 RMS error when predicting channel location and magnitude with the ANN over
 257 a linear regression, with values ranging from 26.5% to over 90% decrease in error.
 258 Moreover, the linear regressions model was generally ineffective at predicting spatial
 259 channel signatures. A ranking of the linear regression weights for all features is given
 260 in Table 2 and Figure 4 over all four training scenarios. In Figure 4, we show the

261 linear regression weights for all features. The last feature shown (19) is the size of
 262 the constant term or bias in the linear regression.

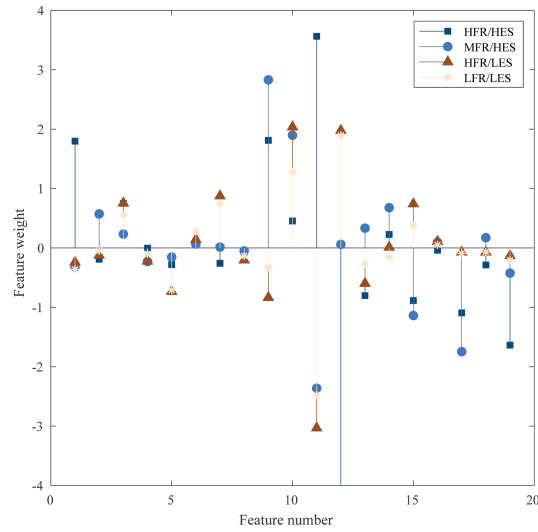


Figure 4: Linear regression weights for all features. The outlying weight on feature 12 is -6.22.

263 As all features were normalized before performing linear regression, we propose that
 264 features that ended with small weights were related to physical attributes which had
 265 little effect on a channel's formation. By this reasoning, we interpret that features
 266 2, 4, 6, 8, 16, and 18 all correspond to physical properties which had little influence.
 267 These features are the area of connected pores, the median length of connections,
 268 the median pore area, the ratio of pore area, the mean ellipse aspect ratio, and the
 269 mean distance between pores. By the same reasoning as above, we interpret fea-
 270 tures with larger weights as proxies for the rocks' physical attributes which broadly
 271 exerted a stronger influence on channel formation. These features include numbers
 272 9 to 12, which correspond to the number of pores, the mean pore perimeter, the
 273 small ellipse perimeter, and the large ellipse perimeter respectively. Of course, this
 274 reasoning of inferring feature influence on enhanced permeability of pre-existing
 275 pathway from linear regression weights is flawed as normalized features with large
 276 outliers may require large scaling to minimize their fitting residuals. Also, as we see
 277 in many cases, linear regression is not an effective predictor of channel formation on
 278 blind test data. Nevertheless, this analysis offers a crude, qualitative first estimate

279 of which features may or may not be important in channel formation prediction
 280 processes within heterogeneous carbonate rocks featuring macropores.

#	Key parameters	Influence
1	Total pore area	Medium
2	Area of connected pores	Low
3	Total length connection	Low
4	Median length connection	Low
5	Mean length connection	Low
6	Median pore area	Low
7	Mean pore area	Medium
8	Ratio pore area	Low
9	Number of pores	High
10	Mean pore perimeter	High
11	Small ellipse perimeter	High
12	Large ellipse perimeter	High
13	Porosity	Medium
14	Number of pore greater than mean size	Low
15	Number of pore greater than median size	Medium
16	Mean ellipse aspect ratio	Low
17	Mean distance between pores	Medium
18	Pore volume rate	Low
19	I/O connection	-

Table 2: Summary of the key parameters used in this study and their apparent relative influence on preferential channel formation.

281 4 Discussion

282 The background density plots (Figure 5) show the distribution of blind predic-
 283 tions generated by the 3,000 neural network simulations, given each combination of
 284 three training experimental regimes (six datasets) and one blind test experimental
 285 regime (two datasets). Intensity ranges from low (blue) to high (yellow) number of

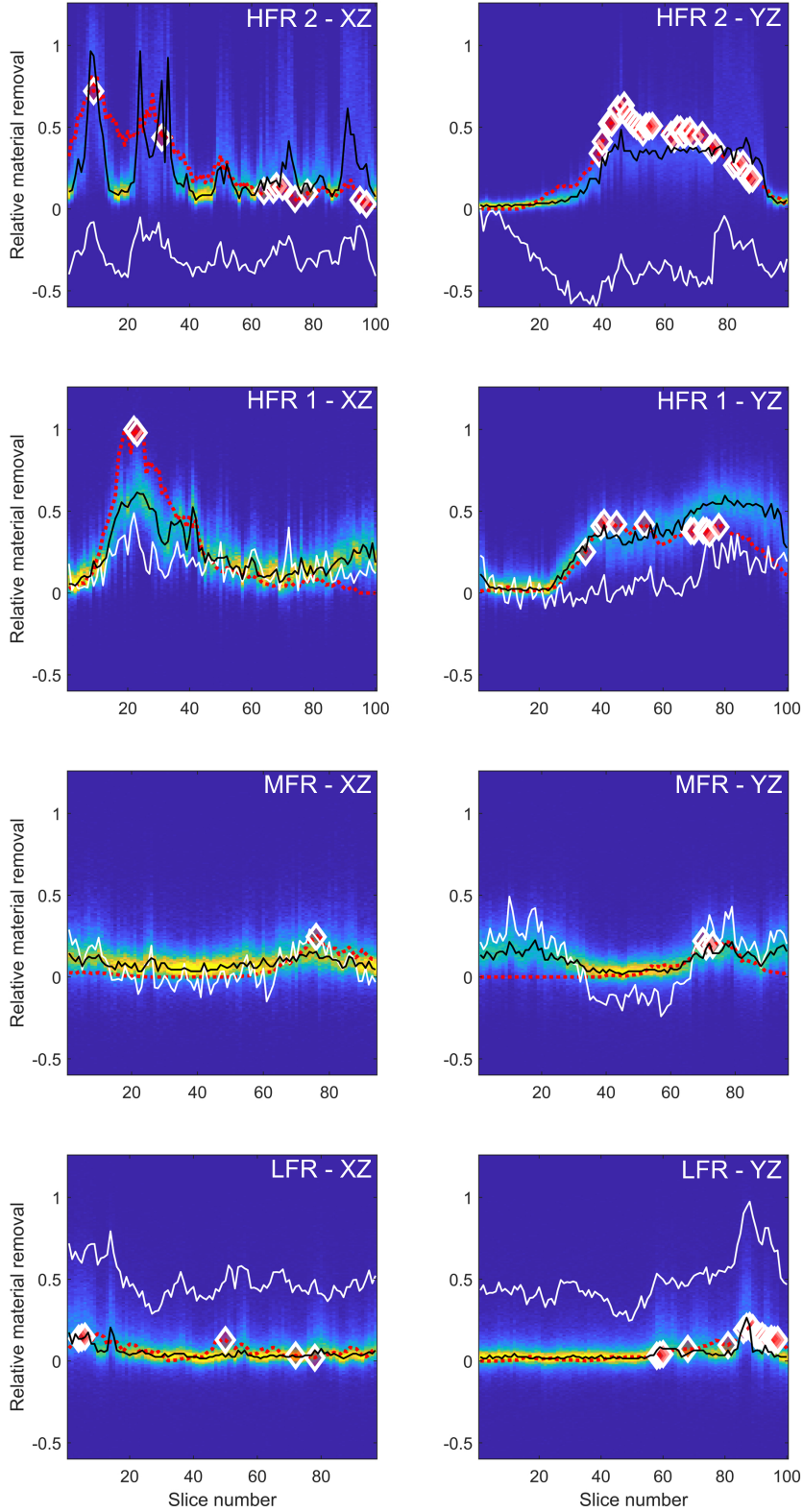


Figure 5: Measured data (red) overlain on density plot of 3,000 trained neural networks' blind test predictions for the four experiments. The white lines show the fitted linear regression models. The black lines represent the best fit for the network blind test predictions. The diamonds are the non-neural network solutions for regions of likelihood for breakthrough independently computed using variable 19 (not included in the neural network predictions).

Core name	ANN RMSE	Linear Reg. RMSE	Difference in RMSE (%)
LFR XZ	0.04	0.45	-90.6
LFR YZ	0.04	0.43	-90.2
HFR 2 YZ	0.13	0.23	-42.5
HFR 2 XZ	0.18	0.27	-35.9
HFR 1 YZ	0.11	0.66	-83.4
HFR 1 XZ	0.20	0.59	-65.7
MFR YZ	0.09	0.19	-51.3
MFR XZ	0.07	0.09	-26.5

Table 3: Percentage of the decrease in root-mean-square-error between linear regression and our ANN solution (respectively white and black lines in Figure 5). Our solution shows an increase in prediction quality of up to $\sim 90\%$.

286 solutions in the bins histogram. The black lines represent the averaged best solu-
287 tions from our predictions. The “true” solutions (signatures) have been plotted in
288 red on top of each result. We observed a generally effective prediction of dissolution
289 channel location and magnitude by our approach for all four training and prediction
290 experiments. There was a notable improvement of accuracy over the linear regres-
291 sion modelling. The spread in the density plot at locations with a large spatial chan-
292 nel signature indicated the sensitivity of neural network training to the particular,
293 random segmentation of validation and training data. The red diamonds on Figure
294 5 indicate where the feature 19 has found an existing pore space connection from
295 sample input to output in the pre-flooded rock. This single feature was an effec-
296 tive predictor for breakthrough and principal channel(s) location. This implied that
297 dissolution channels are likely to occur where there is a pre-existing input/output
298 connection in the rock before flooding. We note this feature only predicted the lo-
299 cation, rather than the magnitude. For this reason, the use of our neural network
300 method was beneficial over using only feature 19.

301 The influence of the key parameters has been assessed through an analysis of the
302 linear regression weights for all the features processed by the ANN (Figure 4). We
303 attributed a rank to a feature by summing, per feature, the weights of each of the

304 four experiments. A feature was ranked “Low” if the sum S was ≤ 1 ; “Medium” if
305 $1 \leq S \leq 2$, and “High” if $S > 2$. The parameters ranked as “High” in Table 2 were
306 assumed important as they reflected how physical (eg. fluid dynamic) and chemical
307 variables (such as reactive transport, the acidity of the fluid, chemical interaction,
308 etc.) could have been influenced by the surface of the pores so that the larger a pore
309 perimeter was, the more important the wall surface in contact with the flooding fluid
310 should have been. These effects were positively impacted by the amount of pores
311 present. This also validated the ellipse shape assigned to each pore as a correct
312 simplification of the general shape of a pore (Tsukrov & Kachanov, 1993; Fournier
313 et al., 2011). We noted that the variables linked to the area of the pores were not
314 ranking higher than “Medium” (and most often “Low”). We explained this by the
315 relatively small importance of the area of the pores. While large pores should have
316 driven more fluid, the large perimeter (likely associated with a large area) guar-
317 anteed more wall-fluid interaction that could have been associated with a higher
318 degree of alteration. This was consistent with Darcy’s law, where the flow will tend
319 to be slower and residence time longer. This was possibly accentuated in the case of
320 travertine rocks by the initial high surface roughness caused by calcite overgrowth
321 in the pores, leading to the very high initial perimeter (although not measurable at
322 the scale of our scans). We also believe that the ANN has made a clear distinction
323 between porosity and number of pores, for reasons similar to that which have been
324 explained above: a large effective porosity could have been associated with large
325 pore areas, while the number of pores remained largely uncorrelated to the area of
326 the pores.

327 **5 Conclusions**

328 This study offers a new way to accurately predict the location and shape of
329 channels formed during water flooding in carbonates, by coupling Artificial Neu-
330 ral Networks (ANNs) and μ CT images. A limited number of studies have already
331 successfully linked these two tools as a segmentation method, and for rock modulus
332 estimation, but none used ANNs for dissolution prediction. While it is commonly
333 stated that the velocity of flow at the inlet of a core sample is the main factor for
334 rock dissolution and/or material removal, this is only part of the story. The find-
335 ings of our work showed that spatial distribution of the porosity evolution can be

336 predicted using only the pore network information held by the rock sample; where
337 the micro- or macro-heterogeneities of the porous medium drive the flow instabili-
338 ties to direct the fluid flow and, as such, chemical removal, towards zones of highest
339 permeability leading to material loss. Our results showed that specific variables
340 stand-out of the ANN analysis, and validate that geometric factors linked to the
341 porosity and pore shape of a rock contain, most of the time, the necessary data for
342 predicting material loss during rock-water flooding. If a linear combination of these
343 μ CT-extracted attributes can successfully predict a rock's spatial channel signature,
344 the weights from the linear regression could be considered indicators of the influence
345 of μ CT-extracted feature in channel formation. While this statement is valid in het-
346 erogeneous travertine rocks, we remain careful with other types of carbonate, or even
347 other types of lithology which have not been tested in this study.

348 **Acknowledgments**

349 The authors would like to thank Petrobras and Shell for their sponsorship of the
350 International Centre for Carbonate Reservoirs (ICCR), and for permission to publish
351 this work from the GeoMeChem project.

352 The data used in this work are available at the following address: [https://](https://doi.org/10.6084/m9.figshare.c.5335454)
353 doi.org/10.6084/m9.figshare.c.5335454 (Brondolo et al., 2021).

354 **References**

- 355 Basheer, I. A., & Hajmeer, M. (2000). Artificial neural networks: fundamentals,
356 computing, design, and application. *Journal of microbiological methods*, *43*(1),
357 3–31.
- 358 Bazin, B., Roque, C., Bouteica, M., et al. (1995). A laboratory evaluation of acid
359 propagation in relation to acid fracturing: Results and interpretation. In *Spe*
360 *europaen formation damage conference*. Society of Petroleum Engineers.
- 361 Bijeljic, B., Muggeridge, A. H., & Blunt, M. J. (2004). Pore-scale modeling of longi-
362 tudinal dispersion. *Water Resources Research*, *40*(11).
- 363 Blunt, M. J., Bijeljic, B., Dong, H., Gharbi, O., Iglauer, S., Mostaghimi, P., ...
364 Pentland, C. (2013). Pore-scale imaging and modelling. *Advances in Water*
365 *Resources*, *51*, 197–216.
- 366 Brondolo, F., Cilli, P., Fraser-Harris, A., Butler, I., Edlmann, K., & McDer-

- 367 mott, C. (2021, Mar). *Machine learning based prediction of channeli-*
368 *sation during dissolution of carbonate rocks.* figshare. Retrieved from
369 [https://figshare.com/collections/Machine_learning_based_prediction](https://figshare.com/collections/Machine_learning_based_prediction_of_channelisation_during_dissolution_of_carbonate_rocks/5335454/1)
370 [_of_channelisation_during_dissolution_of_carbonate_rocks/5335454/1](https://figshare.com/collections/Machine_learning_based_prediction_of_channelisation_during_dissolution_of_carbonate_rocks/5335454/1)
371 doi: 10.6084/m9.figshare.c.5335454
- 372 Budek, A., & Szymczak, P. (2012). Network models of dissolution of porous media.
373 *Physical Review E*, 86(5), 056318.
- 374 Buijse, M., et al. (1997). Mechanisms of wormholing in carbonate acidizing. In *In-*
375 *ternational symposium on oilfield chemistry*. Society of Petroleum Engineers.
- 376 Chauhan, S., Rühaak, W., Khan, F., Enzmann, F., Mielke, P., Kersten, M., & Sass,
377 I. (2016). Processing of rock core microtomography images: Using seven differ-
378 ent machine learning algorithms. *Computers & Geosciences*, 86, 120–128.
- 379 Chen, Y., Fambrough, J., Bartko, K., Li, Y., Montgomery, C., Ortoleva, P., et al.
380 (1997). Reaction-transport simulation of matrix acidizing and optimal acidiz-
381 ing strategies. In *International symposium on oilfield chemistry*. Society of
382 Petroleum Engineers.
- 383 Cortina-Januchs, M., Quintanilla-Dominguez, J., Vega-Corona, A., Tarquis, A., &
384 Andina, D. (2011). Detection of pore space in ct soil images using artificial
385 neural networks. *Biogeosciences*, 8(2), 279–288.
- 386 Daccord, G., Lenormand, R., & Lietard, O. (1993). Chemical dissolution of a porous
387 medium by a reactive fluid—i. model for the “wormholing” phenomenon.
388 *Chemical Engineering Science*, 48(1), 169–178.
- 389 Daccord, G., Lietard, O., & Lenormand, R. (1993). Chemical dissolution of a porous
390 medium by a reactive fluid—ii. convection vs reaction, behavior diagram.
391 *Chemical engineering science*, 48(1), 179–186.
- 392 Daccord, G., Touboul, E., Lenormand, R., et al. (1989). Carbonate acidizing: to-
393 ward a quantitative model of the wormholing phenomenon. *SPE production*
394 *engineering*, 4(01), 63–68.
- 395 Dierick, M., Masschaele, B., & Van Hoorebeke, L. (2004). Octopus, a fast and user-
396 friendly tomographic reconstruction package developed in labview®. *Measure-*
397 *ment Science and Technology*, 15(7), 1366.
- 398 Fournier, F., Leonide, P., Biscarrat, K., Gallois, A., Borgomano, J., & Foubert, A.
399 (2011). Elastic properties of microporous cemented grainstones. *Geophysics*,

- 400 76(6), E211–E226.
- 401 Fredd, C., Fogler, H. S., et al. (1996). Alternative stimulation fluids and their im-
402 pact on carbonate acidizing. In *Spe formation damage control symposium*. So-
403 ciety of Petroleum Engineers.
- 404 Fredd, C. N., & Fogler, H. S. (1998). Influence of transport and reaction on worm-
405 hole formation in porous media. *AIChE journal*, 44(9), 1933–1949.
- 406 Frick, T., Mostofizadeh, B., Economides, M., et al. (1994). Analysis of radial core
407 experiments for hydrochloric acid interaction with limestones. In *Spe formation*
408 *damage control symposium*. Society of Petroleum Engineers.
- 409 Golfier, F., Zarconne, C., Bazin, B., Lenormand, R., Lasseux, D., & QUINTARD,
410 M. (2002). On the ability of a darcy-scale model to capture wormhole forma-
411 tion during the dissolution of a porous medium. *Journal of fluid Mechanics*,
412 457, 213–254.
- 413 Hoefner, M., & Fogler, H. S. (1988). Pore evolution and channel formation during
414 flow and reaction in porous media. *AIChE Journal*, 34(1), 45–54.
- 415 Huang, T., Hill, A., Schechter, R., et al. (1997). Reaction rate and fluid loss: the
416 keys to wormhole initiation and propagation in carbonate acidizing. In *Inter-*
417 *national symposium on oilfield chemistry*. Society of Petroleum Engineers.
- 418 Huang, T., Zhu, D., & Hil, A. (1999). Prediction of wormhole population density in
419 carbonate matrix acidizing. In *Spe european formation damage conference*. So-
420 ciety of Petroleum Engineers.
- 421 Hudson Beale, M., Hagan, M. T., & Demuth, H. B. (2018). *Impress - supporting ed-*
422 *ucation across europe*. Retrieved from [https://uk.mathworks.com/help/pdf](https://uk.mathworks.com/help/pdf_doc/deeplearning/nnet_ref.pdf)
423 [_doc/deeplearning/nnet_ref.pdf](https://uk.mathworks.com/help/pdf_doc/deeplearning/nnet_ref.pdf)
- 424 Hung, K., Hill, A., Sepehrnoori, K., et al. (1989). A mechanistic model of wormhole
425 growth in carbonate matrix acidizing and acid fracturing. *Journal of petroleum*
426 *technology*, 41(01), 59–66.
- 427 Liu, X., Ormond, A., Bartko, K., Ying, L., & Ortoleva, P. (1997). A geochemical
428 reaction-transport simulator for matrix acidizing analysis and design. *Journal*
429 *of Petroleum Science and Engineering*, 17(1-2), 181–196.
- 430 Luquot, L., Hebert, V., & Rodriguez, O. (2016). Calculating structural and geomet-
431 rical parameters by laboratory measurements and x-ray microtomography: a
432 comparative study applied to a limestone sample before and after a dissolution

- 433 experiment. *Solid Earth*, 7(2).
- 434 Menke, H., Bijeljic, B., & Blunt, M. (2017). Dynamic reservoir-condition microto-
435 mography of reactive transport in complex carbonates: Effect of initial pore
436 structure and initial brine ph. *Geochimica et Cosmochimica Acta*, 204, 267–
437 285.
- 438 Ridler, T., Calvard, S., et al. (1978). Picture thresholding using an iterative selection
439 method. *IEEE transactions on Systems, Man and Cybernetics*, 8(8), 630–632.
- 440 Schindelin, J., Arganda-Carreras, I., Frise, E., Kaynig, V., Longair, M., Pietzsch, T.,
441 ... others (2012). Fiji: an open-source platform for biological-image analysis.
442 *Nature methods*, 9(7), 676.
- 443 Sonmez, H., Gokceoglu, C., Nefeslioglu, H., & Kayabasi, A. (2006). Estimation of
444 rock modulus: for intact rocks with an artificial neural network and for rock
445 masses with a new empirical equation. *International Journal of Rock Mechan-*
446 *ics and Mining Sciences*, 43(2), 224–235.
- 447 Steefel, C. I., & Lasaga, A. C. (1990). Evolution of dissolution patterns. In *Chemical*
448 *modeling of aqueous systems ii* (p. 212-225). American Chemical Society. Re-
449 trieved from <https://pubs.acs.org/doi/abs/10.1021/bk-1990-0416.ch016>
450 doi: 10.1021/bk-1990-0416.ch016
- 451 Terzaghi, K. (1951). *Theoretical soil mechanics*. Chapman And Hall, Limited.; Lon-
452 don.
- 453 Tsukrov, I., & Kachanov, M. (1993). Solids with holes of irregular shapes: effective
454 moduli and anisotropy. *International Journal of Fracture*, 64(1), R9–R12.
- 455 Walle, L., Papamichos, E., et al. (2015). Acidizing of hollow cylinder chalk speci-
456 mens and its impact on rock strength and wormhole network structure. In *49th*
457 *us rock mechanics/geomechanics symposium*. American Rock Mechanics Asso-
458 ciation.
- 459 Wang, Y., Hill, A., Schechter, R., et al. (1993). The optimum injection rate for ma-
460 trix acidizing of carbonate formations. In *Spe annual technical conference and*
461 *exhibition*. Society of Petroleum Engineers.